

The formation of entropy cores in non-radiative galaxy cluster simulations: SPH versus AMR

C. Power^{1*}, J. I. Read² & A. Hobbs³

¹*International Centre for Radio Astronomy Research, University of Western Australia, 35 Stirling Highway, Crawley, Western Australia 6009, Australia*

²*Department of Physics, University of Surrey, Guildford, GU2 7XH, Surrey, United Kingdom*

³*Institute for Astronomy, Department of Physics, ETH Zürich, Wolfgang-Pauli-Strasse 16, CH- 8093, Zürich, Switzerland*

ABSTRACT

We simulate the formation and evolution of a massive galaxy cluster in a Λ CDM Universe using three different approaches to solving the equations of hydrodynamics in the absence of radiative cooling: one based on the ‘classic’ Smoothed Particle Hydrodynamics (SPH) method; one based on a novel SPH algorithm with a higher order dissipation switch (SPHS); and one based on an adaptive mesh refinement (AMR) method. We find that SPHS and the AMR code are in excellent agreement with one another: in both, the spherically averaged entropy profile forms a well-defined core that rapidly converges with increasing mass and force resolution. By contrast, in agreement with previous work, SPH exhibits rather different behaviour. At low redshift, the entropy profile shows a systematic decrease with decreasing cluster-centric radius, converging on ever lower central entropy with increasing resolution. At higher redshift ($z \sim 1$), SPH is in better agreement with the other codes but shows much poorer numerical convergence. We trace the reason for these discrepancies to a known artificial surface tension in SPH that appears at phase boundaries. At early times, the passage of massive substructures close to the cluster centre during its violent assembly stirs and shocks the gas to build up an entropy core. At late times, the artificial surface tension causes low entropy gas – that ought to mix with the higher entropy gas – to sink artificially to the centre of the cluster.

We use SPHS – in which we can fully control the amount of numerical dissipation – to study the contribution of numerical versus physical dissipation on the resultant entropy core. We argue that numerical dissipation is required to ensure single-valued fluid quantities in converging flows. However, provided this dissipation occurs only at the resolution limit, and provided that it does not propagate errors to larger scales, its effect is benign. There is no requirement to build ‘sub-grid’ models of unresolved turbulence for galaxy cluster simulations. We conclude that entropy cores in non-radiative simulations of galaxy clusters are physical, resulting from entropy generation in shocked gas during the cluster assembly process. This finally puts to rest the long-standing puzzle of cluster entropy cores in AMR simulations versus their apparent absence in classic SPH simulations.

Key words:

1 INTRODUCTION

Cosmological simulations are an established and powerful tool for studying the origin of cosmic structure and the formation of galaxies (e.g. Springel et al. 2006). The formation and evolution of cosmic structure is assumed to be driven by a collisionless dark matter component, which forms massive collapsed structures – so-called haloes – that provide the potential wells within which gas cools and condenses to form galaxies (White & Rees 1978). The clustering and dynamics of the dark matter component has been studied in exhaustive detail over the last three decades and the N -body technique can be considered mature (see, for example, the recent

review of Dehnen & Read 2011). By contrast, the behaviour of the gas component is less secure. In part, this reflects uncertainty about the physical processes that are important (Thacker & Couchman 2000; Mayer et al. 2008; Scannapieco et al. 2012), but it also reflects uncertainty about the manner in which the Euler equations are solved.

In particular, Agertz et al. (2007) found that the two most popular methods for solving the Euler equations in the literature – Smoothed Particle Hydrodynamics (SPH; Lucy 1977; Gingold & Monaghan 1977; Monaghan 1992), and Adaptive Mesh Refinement (AMR; Berger & Oliger 1984; Berger & Colella 1989; Bryan & Norman 1997; Khokhlov 1998; Fryxell et al. 2000; Teyssier 2002) – give very different dissolution rates for a cold dense blob of gas moving at supersonic speed through a hot

* chris.power@icrar.org

medium: in ‘classic’ SPH¹, the blobs survive much longer than their AMR counterparts. Read et al. (2010) showed that this owes to two different problems with classic SPH: a leading order error in the momentum equation (Dilts 1999; Inutsuka 2002); and an artificial surface tension at phase boundaries (Ritchie & Thomas 2001; Price 2008; Wadsley et al. 2008).

Over the past few years, there has been a welcome proliferation of new SPH “flavours” and Lagrangian hydrodynamic methods designed to address the above problems (Springel 2010; Heß & Springel 2010; Gaburov & Nitadori 2010; Abel 2011; Murante et al. 2011; Read & Hayfield 2012; Kawata et al. 2013; Saitoh & Makino 2013; Hopkins 2013). These give significantly improved results on hydrodynamical test problems that have known analytic solutions (e.g. Read & Hayfield 2012). When applied to astrophysical problems like galaxy formation, the results can also be quite different from the classic SPH simulations reported in the literature to date (Sijacki et al. 2012; Hobbs et al. 2012). This suggests that – in addition to the problem of unresolved or ‘sub-grid’² physics (Scannapieco et al. 2012) – the choice of hydrodynamic solver matters.

Despite the above progress, a much older tension between SPH and AMR codes has eluded a complete explanation. Frenk et al. (1999) simulated the formation of a non-radiative massive galaxy cluster using 12 different codes, finding that the SPH codes and the AMR³ code converged on very different solutions from one another. In particular, the differences were most stark in the radial entropy profile of the gas, defined as:

$$S(R) = \log \left[T_{\text{gas}}(R) / \rho_{\text{gas}}(R)^{2/3} \right] \quad (1)$$

where R is the spherical radius with respect to the cluster centre of mass; T_{gas} is the gas temperature; and ρ_{gas} is the gas density. The SPH simulations appeared to converge on an ever lower central entropy as the force and mass resolution were increased, while the AMR simulation appeared to converge on a central constant entropy core. These results have been confirmed by several studies since (Voit et al. 2005; O’Shea et al. 2005; Dolag et al. 2005; Wadsley et al. 2008; Mitchell et al. 2009). Wadsley et al. (2008) simulated gas in a galaxy cluster using the Frenk et al. (1999) initial conditions using classic SPH with and without diffusion and concluded that lack of diffusion and particularly mixing in classic SPH gives rise to the non-convergent behaviour seen in earlier studies (see also Price 2008). Mitchell et al. (2009) studied mergers between idealised galaxy clusters and traced the discrepancy to the artificial surface tension and the associated lack of multiphase fluid mixing in classic SPH, in agreement with Wadsley et al. (2008). Sijacki et al. (2011) arrive at a similar conclusion by comparing classic SPH with a new moving mesh code, *Arepo*. However, while it is likely that the classic SPH result is incorrect, this does not automatically imply that the AMR results are correct. Vazza (2011) report significant variation in the entropy profile for the same AMR code (*Enzo*) when run with different refinement

criteria, force resolution, and choice of energy equation. The refinement criteria appears to be most critical: depending on whether they refine on density or additionally on velocity jumps, they can produce entropy cores that differ in magnitude by up to a factor of two. Furthermore, this difference remains even when the numerical resolution is increased⁴. In addition to variations in the entropy profile due to a particular flavour of AMR, differences are also seen when comparing the AMR results to that of the moving mesh code *Arepo*. Springel (2010) report an entropy core that is significantly lower than that found in AMR codes (e.g. compare Figure 45 of Springel 2010 with Figure 18 of Frenk et al. 1999 or Figure 5 of Voit et al. 2005).

The above discrepancies between different numerical techniques are important. Since the advent of space-based X-ray satellites, it has been known that real galaxy clusters split into two broad observational classes: *cooling-core* (CC) clusters that have very low central entropy, and *non-cooling-core* (NCC) clusters that have an approximately constant entropy core in the centre (e.g. McCarthy et al. 2008). If different methods for solving the non-radiative Euler equations lead to a CC (SPH) or NCC (AMR) cluster, then we are unable to determine the real physical processes that drive this dichotomy in nature. A proper understanding of the thermodynamic state of cluster gas is vital for using clusters as cosmological probes (e.g. Gunn & Gott 1972; Voit 2005); as probes of the baryon content of the Universe (e.g. Giodini et al. 2009); or as probes of dark matter through their hot X-ray emitting gas (e.g. Cavaliere & Fusco-Femiano 1976; Hughes 1989; Vikhlinin et al. 2006).

In this paper, we revisit the problem of modelling non-radiative cosmological galaxy clusters using a new flavour of SPH – SPHS – that is designed to resolve two key problems with SPH: (i) multivalued pressures at flow boundaries that lead to a numerical surface tension; and (ii) poor force accuracy in shearing flows (Read & Hayfield 2012). The former problem is cured by introducing a higher order dissipation switch that detects, in advance, when particles are going to converge⁵. If this happens, conservative dissipation is switched on for all advected fluid quantities (i.e. artificial thermal conductivity, artificial viscosity, etc.). The dissipation is switched off again once particles are no longer converging. This ensures that all fluid quantities are single-valued throughout the flow by construction. The second problem is cured by moving to higher order stable kernels that can support larger neighbour numbers (Read et al. 2010; Dehnen & Aly 2012). We use the default kernel choice from Read et al. (2010): the HOCT4 kernel with 442 neighbours. Read & Hayfield (2012) demonstrated that SPHS performs very well on a broad range of hydrodynamic test problems including the Sod shock tube, Sedov-Taylor blast wave, Gresho vortex, and the high density contrast Kelvin-Helmholtz instability test, giving excellent agreement with analytic expectations. A key advantage of the SPHS method is that we can explicitly con-

¹ We define this to be the form of SPH implemented in the *Gadget-2* code, and similar (Springel 2005).

² We refer, as is common in the literature, to physics below the resolution limit of a simulation as being ‘sub-grid’ – even though in SPH there are no actual grid cells. Such physics must either be omitted or modelled phenomenologically, with advantages and disadvantages to both approaches.

³ In fact, only one code in the study utilised adaptive mesh refinement techniques (Bryan et al. 1995). However, as a result, this was the only Eulerian mesh code that was capable of resolving the entropy core.

⁴ This may simply imply that some refinement criteria are better than others. When comparing with fixed-grid simulations, Mitchell et al. (2009) find that the standard density-refinement AMR gives excellent agreement. However, this test was performed only for a simplified set-up using just one single cluster merger; convergence is more difficult to achieve for the full cosmological case where additional substructure is present in the initial conditions as the resolution is increased. To our knowledge, comparisons between high resolution fixed grid and AMR simulations of non-radiative cosmological galaxy clusters have not yet been performed

⁵ This is similar to a switch proposed first by Cullen & Dehnen (2010) but switching on *all* advected fluid quantities, not just the artificial viscosity.

trol the amount of numerical dissipation. This allows us to measure how dissipation at the resolution limit feeds back to larger resolved scales in the simulation.

We test the convergence of our results with increasing mass and force resolution, the sensitivity to the numerical dissipation parameters, and present explicit comparisons with an AMR code RAMSES (Teyssier 2002). In performing these numerical experiments, we seek to address three key questions:

- (i) What is the origin of the discrepancy between the classic SPH and the AMR results?
- (ii) Do resolved scales in non-radiative simulations of galaxy cluster formation care about the details of dissipation (physical or numerical) on unresolved scales?
- (iii) What is the role of gravitational shock heating as an entropy generation mechanism in galaxy clusters?

This paper is organised as follows. In §2, we describe the different numerical methods – ‘classic’ SPH, SPHS and AMR – used in this work. In §3, we describe our simulation suite. In §4, we present our results. In §5, we return to the three key questions posed above and discuss the meaning of our results for real galaxy clusters in the Universe. Finally, in §6 we present our conclusions.

2 METHODS

2.1 ‘Classic’ SPH

We adopt the fully conservative ‘entropy’ form of SPH described in Springel & Hernquist (2002). The discretised Euler equations are:

$$\rho_i = \sum_j^N m_j W_{ij}(|\mathbf{r}_{ij}|, h_i) \quad (2)$$

$$\frac{d\mathbf{v}_i}{dt} = - \sum_j^N m_j \left[f_i \frac{P_i}{\rho_i^2} \nabla_i W_{ij}(h_i) + f_j \frac{P_j}{\rho_j^2} \nabla_i W_{ij}(h_j) \right] \quad (3)$$

and:

$$P_i = A_i \rho_i^\gamma \quad (4)$$

Here m_i is the mass of particle i ; \mathbf{v}_i is the velocity; P_i is the pressure; ρ_i is the density; A_i is a function that is monotonically related to the entropy (hereafter referred to as the ‘entropy’); W is a symmetric kernel that obeys the normalisation condition:

$$\int_V W(|\mathbf{r} - \mathbf{r}'|, h) d^3 r' = 1, \quad (5)$$

and the property (for smoothing length h):

$$\lim_{h \rightarrow 0} W(|\mathbf{r} - \mathbf{r}'|, h) = \delta(|\mathbf{r} - \mathbf{r}'|), \quad (6)$$

where $\mathbf{r}_{ij} = \mathbf{r}_j - \mathbf{r}_i$ is the vector position of the particle relative to the centre of the kernel; and the function f_i in equation 3 is a correction factor that ensures energy conservation for varying smoothing lengths:

$$f_i = \left(1 + \frac{h_i}{3\rho_i} \frac{\partial \rho_i}{\partial h_i} \right)^{-1} \quad (7)$$

Note that we do not use the above conservative momentum equation in SPHS since it leads to larger force errors with only a modest improvement in energy conservation (at least when applied to

galaxy and galaxy cluster formation simulations; see Read et al. (2010) and Read & Hayfield (2012) for further details).

We use a variable smoothing length h_i as in Springel & Hernquist (2002) that is adjusted to obey the following constraint equation:

$$\frac{4\pi}{3} h_i^3 n_i = N_n \quad ; \text{ with } \quad n_i = \sum_j^N W_{ij} \quad (8)$$

where N_n is the typical neighbour number (the number of particles inside the smoothing kernel, W). The above constraint equation gives fixed mass inside the kernel if particle masses are all equal. We use a standard cubic spline (CS) kernel with $N_n = 40$ neighbours.

There is no dissipation switching and $\alpha = \alpha_{\max} = \text{const.} = 1$ always. There is also no dissipation in entropy; the only numerical dissipation applied is the artificial viscosity. This prevents multivalued momenta from occurring, but not multivalued entropy or pressure (e.g., Read et al. 2010).

2.2 SPH with a higher order dissipation Switch (SPHS)

SPHS minimises force errors in the discretised hydrodynamic equations of motion (cf. Read et al. 2010), and so the key difference with respect to classic SPH arises in the momentum equation, which is recast as:

$$\frac{d\mathbf{v}_i}{dt} = - \sum_j^N \frac{m_j}{\rho_i \rho_j} [P_i + P_j] \nabla_i \bar{W}_{ij} \quad (9)$$

where $\bar{W}_{ij} = \frac{1}{2} [W_{ij}(h_i) + W_{ij}(h_j)]$ is a symmetrised smoothing kernel.

We adopt the ‘HOCT4’ smoothing kernel with 442 neighbours as this gives significantly improved force accuracy and convergence (Read et al. 2010; Read & Hayfield 2012):

$$W = \frac{N}{h^3} \begin{cases} Px + Q & 0 < x \leq \kappa \\ (1-x)^4 + (\alpha-x)^4 + (\beta-x)^4 & \kappa < x \leq \beta \\ (1-x)^4 + (\alpha-x)^4 & \beta < x \leq \alpha \\ (1-x)^4 & x \leq 1 \\ 0 & \text{otherwise} \end{cases} \quad (10)$$

with $N = 6.515$, $P = -2.15$, $Q = 0.981$, $\alpha = 0.75$, $\beta = 0.5$ and $\kappa = 0.214$.

In addition to the above equations of motion, numerical dissipation is switched on if particles are converging. This avoids multivalued fluid quantities occurring at the point of convergent flow. Without such dissipation, the resulting multivalued pressures drive waves through the fluid that propagate large numerical errors and spoil convergence. The switch is given by:

$$\alpha_{\text{loc},i} = \begin{cases} \frac{h_i^2 |\nabla(\nabla \cdot \mathbf{v}_i)|}{h_i^2 |\nabla(\nabla \cdot \mathbf{v}_i)| + h_i |\nabla \cdot \mathbf{v}_i| + n_s c_i} \alpha_{\max} & \nabla \cdot \mathbf{v}_i < 0 \\ 0 & \text{otherwise} \end{cases} \quad (11)$$

where $\alpha_{\text{loc},i}$ describes the amount of dissipation for a given particle i , in the range $[0, \alpha_{\max} = 1]$; c_i is the sound speed of particle i ; and $n_s = 0.05$ is a ‘noise’ parameter that determines the magnitude of velocity fluctuations that trigger the switch. Equation 11 turns on dissipation if $\nabla \cdot \mathbf{v}_i < 0$ (convergent flow) and if

the magnitude of the spatial derivative of $\nabla \cdot \mathbf{v}_i$ is large as compared to the local divergence (i.e., if the flow is going to converge). The key advantage as compared to most other switches in the literature is that it acts as an early warning system, switching on *before* large numerical errors propagate throughout the fluid (see also Cullen & Dehnen 2010). The second derivatives of the velocity field are calculated using high order polynomial gradient estimators described in Maron & Howes (2003) and Read & Hayfield (2012). We use the above switch to turn on dissipation in all advected fluid quantities – i.e., the momentum (artificial viscosity) and entropy (artificial thermal conductivity). Once the trajectories are no longer converging, the dissipation parameter decays back to zero on a timescale $\sim h_i/c_i$. The dissipation equations are fully conservative and described in detail in Read & Hayfield (2012). The key free numerical parameter is α_{\max} that sets the rate of dissipation that occurs when particle trajectories attempt to cross. This parameter allows us to control the amount of resolution-scale dissipation from zero (similar to classic SPH), up to large values ($\alpha_{\max} \sim 1$ is the natural choice since this leads to single-valued fluid quantities on a timescale comparable to the particle trajectory convergence time). We might hope that the results on resolved scales do not care about the amount or form of dissipation that occurs at the resolution limit, since such dissipation moves to ever smaller scales as the resolution is increased. Indeed, in test problems SPHS converges independently of the choice of α_{\max} so long as it is large enough to avoid multi-valued pressures (Read & Hayfield 2012). However, for complex non-linear problems this is not entirely clear. Dissipation on unresolved scales could in principle affect the results on resolved scales if it causes an upwards transfer of information in the form of pressure waves, for example. This would manifest as numerically ‘converged’ results on resolved scales that depend on the magnitude and form of the numerical dissipation parameters. We test this explicitly using SPHS in §4.

2.3 AMR

We used the RAMSES adaptive mesh refinement (AMR) code of Teyssier (2002). The evolution of the gas is followed using a second-order unsplit Godunov scheme for the Euler equations. Collisionless N -body particles are evolved using a particle-mesh solver with a Cloud-In-Cell interpolation. The coarse mesh is refined using a quasi-Lagrangian strategy, such that cells are refined when more than 8 dark matter particles lie in a cell or if the baryon density is larger than 8 times the initial dark matter resolution. When refined, cells are divided into 8 smaller cubic cells, giving a factor of 2 increase in spatial resolution. These smaller cells may be refined further, up to a maximum level of refinement defined by the user. Timesteps are adapted to the levels of refinement so that the timestep for cells at refinement level ℓ is twice as long as the timestep at level $\ell + 1$.

3 SIMULATIONS

Parent Simulation Our parent N -body simulation follows structure formation in a periodic volume of side $L_{\text{box}} = 150h^{-1}\text{Mpc}$ containing 150^3 particles in the ΛCDM model with cosmological $\Omega_0 = 0.7$, $\Omega_\Lambda = 0.3$, $h = 0.7$, and a normalisation of $\sigma_8 = 0.9$. The particle mass $m_p \simeq 8.3 \times 10^{10}h^{-1}\text{M}_\odot$ ensures that the most massive clusters likely to form in a volume of this size will contain $\sim 10^4$ particles within their virial radius r_{vir} at $z=0$; this is

sufficient to define the region to be resimulated at higher mass resolution.

We used the parallel TreePM code GADGET2 (Springel 2005) with constant comoving gravitational softening $\epsilon = 20h^{-1}\text{kpc}$ to run the simulation and constructed group catalogues using AHF (AMIGA’s Halo Finder; cf. Knollmann & Knebe 2009). For each halo in the AHF catalogue we determined the centre-of-density \vec{r}_{cen} using the iterative “shrinking spheres” method described in Power et al. 2003 and we identified this as the halo centre. From this, we calculated the halo’s virial radius r_{vir} , which we define as the radius within which the mean interior density is Δ_{vir} times the critical density of the Universe at that redshift, $\rho_c(z) = 3H^2(z)/8\pi G$, where $H(z)$ and G are the Hubble parameter at z and the gravitational constant respectively. The corresponding virial mass M_{vir} is

$$M_{\text{vir}} = \frac{4\pi}{3} \Delta_{\text{vir}} \rho_c r_{\text{vir}}^3. \quad (12)$$

where we adopt $\Delta_{\text{vir}}=200$, independent of redshift.

Galaxy Cluster Resimulation We chose to resimulate the most massive halo to form in our parent simulation with both gas and dark matter – corresponding to a galaxy cluster with a virial mass of $M_{\text{vir}} \simeq 6 \times 10^{15}h^{-1}\text{M}_\odot$ ($N_{\text{vir}} \simeq 7200$ particles) and virial radius of $R_{\text{vir}} \simeq 1.35h^{-1}\text{Mpc}$ at $z=0$. The resimulation technique allows us to target our computational effort so that we can employ high mass and force resolution in a sub-volume of the original parent simulation, whilst also capturing the large scale tidal effects due to all the other matter in the Universe. To set up the initial conditions for our resimulations, we took the following steps;

- (i) We identified all particles within a volume of radius $\sim 3.5R_{\text{vir}}$ centred on the centre of density \vec{r}_{cen} of the cluster halo at $z=0$ in the parent simulation and determined their positions in its initial conditions at the starting redshift $z_{\text{start}}=74$.
- (ii) Using the particle velocities and z_{start} , we applied an inverse Zel’dovich transformation to obtain the particle positions at $z = \infty$, from which we determined the spatial extent of the initial Lagrangian volume. This volume defines the central region of a multi-level mask for the high resolution region.
- (iii) We populated this simulation volume with particles with a number density set by our high resolution mask; the number density of particles within the central region of the mask is highest – set by the desired mass resolution of the resimulation – and declines in subsequent levels of the mask, such that the mass resolution coarsens with increasing distance from the central region. For hydrodynamical simulations of the kind described in this paper, we include both gas and dark matter particles within the central region, with number densities fixed by the cosmological baryon and dark matter density parameters $\Omega_b = 0.04$ and $\Omega_{\text{DM}} = 0.26$.
- (iv) We imposed two sets of density perturbations on this composite particle distribution. The first set correspond to the original set of perturbations that were present in the initial conditions of the parent simulation, with minimum and maximum wavenumbers, $k_{\min} = 2\pi/L_{\text{box}}$ and $k_{\max} = \pi N_p/L_{\text{box}}$, and the second set corresponds to perturbations that were not present in the initial conditions, $k_{\min} = 2\pi/L_{\text{hires}}$ and $k_{\max} = \pi N_{\text{hires}}/L_{\text{hires}}$. Here L_{box} and L_{hires} are the side-lengths of the parent volume and box encompassing the high resolution patch respectively, and N_p and N_{hires} are the number of dark matter particles on a side in these boxes.
- (v) From these perturbations we constructed the initial baryon

density perturbation field $\delta_b(\vec{x}) = \rho/\bar{\rho} - 1$ at mesh points \vec{x} and used the Zel'dovich approximation to compute the velocity field $\vec{v}(\vec{x})$. From these we initialised gas and dark matter particle positions and velocities.

We used the TreePM N -body SPH code GADGET3, in which we have implemented SPHS, to run the bulk of our simulations. Gravitational force softenings for both the dark matter and the gas were chosen in accordance with the optimal criterion of $\epsilon_{\text{opt}} = 4 r_{\text{vir}}/\sqrt{N_{\text{vir}}}$ of Power et al. (2003).

For comparison, we also ran a subset of the simulations using the public version of the AMR code RAMSES. RAMSES takes as input baryon density perturbation and velocity fields on uniform cubic meshes – the coarser meshes capture the influence of the large-scale gravitational field while the finest mesh – in combination with a refinement map that tells RAMSES where to place its initial refinements – corresponds to the high resolution region. We ran two simulations – one with a minimum level of refinement of $\ell=7$, the other with $\ell=8$, and in both cases we fixed the maximum level of refinement at $\ell=15$. These correspond to mesh cell lengths of $\Delta=L_{\text{hires}}/2^\ell \sim 0.3$ (0.16) $h^{-1}\text{Mpc}$ for $\ell=7$ (8), and $\Delta \sim 0.001 h^{-1}\text{Mpc}$ for $\ell=15$. In both cases we used a criterion of `m_refine=8` (dark matter particles or factor increase in the initial gas mass resolution) to trigger new refinements.

4 RESULTS

In the following subsections we compare the results of our SPH, SPHS and AMR runs. The focus of our analysis is on the entropy of the cluster gas, which we define according to Equation (1). We construct our spherically averaged entropy profiles by defining the cluster centre of density \vec{r}_{cen} using the shrinking spheres method (cf. Power et al. 2003), sorting particles by cluster-centric radius, and assigning them to 25 spherical logarithmic bins equally spaced between $R_{\text{min}} = 0.01 R_{\text{vir}}$ and R_{vir} , where R_{vir} is defined according to Equation (12).

4.1 Comparison of SPH and SPHS

Visual Impression In Figure 1 we show the projected gas density distribution within $15 h^{-1}\text{Mpc}$ cubes centred on the cluster at $z=0$. The top (bottom) panels correspond to the SPH (SPHS) runs, while the left (right) hand panels correspond to the results of the $\times 32$ and $\times 128$ (cf. Table 4.1).

There are several points worthy of note in this figure. First, the large-scale spatial distribution of gas is in very good agreement between runs – the cluster resides at the intersection of several filaments, and the positions and spatial extents of massive gas clumps are consistent across schemes and mass resolutions. Second, and in contrast to first point, the spatial distribution of gas on small scales is noticeably different between SPH and SPHS – the number of small dense knots in the SPH run is greater than in the SPHS run, and gas clumps are more diffuse and extended in the SPHS runs. Third, increasing mass resolution has a more striking effect in the SPH runs, with the number of dense knots increasing in proportion to the increase in mass resolution, whereas this is less obvious in the SPHS runs.

We quantify these second and third points by carrying out a friends-of-friends analysis of the gas density field in the high resolution region, adopting a linking length of $b=0.2$ times the mean inter-particle separation to compare both the abundance and diffuse

Table 1. Cluster Properties at $z=0$. M_{vir} is the virial mass of the halo, expressed in units of $10^{15} h^{-1} \text{M}_\odot$, assuming $\Delta_{\text{vir}}=200$; R_{vir} is the virial radius, in units of $h^{-1} \text{Mpc}$; N_{tot} and N_{gas} are the total number of particles (i.e. gas and dark matter) and the number of gas particles within R_{vir} ; and f_{gas} is the baryon fraction $f_{\text{bar}} = M_{\text{vir,gas}}/M_{\text{vir}}$.

	M_{vir} $10^{15} h^{-1} \text{M}_\odot$	R_{vir} $h^{-1} \text{Mpc}$	N_{DM}	N_{gas}	f_{bar}
SPH					
$\times 2$	6.05	1.375	26430	12427	0.1201
$\times 8$	6.01	1.372	103897	48079	0.1170
$\times 32$	6.15	1.383	424138	195903	0.1166
$\times 64$	6.23	1.389	856379	392356	0.1151
$\times 128$	6.21	1.388	1716394	791771	0.1164
$\times 256$	6.21	1.387	3425723	1581677	0.1166
SPHS					
$\times 2$	6.03	1.374	26818	12938	0.1254
$\times 8$	5.96	1.369	107209	52556	0.1289
$\times 32$	6.20	1.387	445748	218686	0.1290
$\times 64$	6.26	1.391	898319	438296	0.1278
$\times 128$	6.20	1.386	1785832	876886	0.1292
$\times 256$	6.24	1.389	3578077	1748769	0.1282
AMR					
128	4.25	1.222	25786	-	0.1397
256	4.35	1.232	210674	-	0.1424

nature of the gas clumps that form. There are comparable numbers of FOF-identified clumps in the SPH and SPHS $\times 8$ run, with the number of clumps declining as $\sim N_{\text{FOF}}^{-0.5}$ for clumps containing in excess of $N_{\text{FOF}} \sim 50$ particles. For the $\times 32$ runs, we identify ~ 2 -3 times as many gas clumps containing in excess of 50 particles in the SPH run when compared to the SPHS run. For $N_{\text{FOF}} \gtrsim 50$ particles, there is good agreement between the numbers of SPHS clumps in the $\times 8$, 32 and 64 runs, with $\sim N_{\text{FOF}}^{-0.5}$ for increasing N_{FOF} , whereas the numbers of SPH clumps increases with increasing resolution.

In Figure 2 we focus on the inner $5 h^{-1}\text{Mpc}$ (middle panels) and $2 h^{-1}\text{Mpc}$ (bottom panels) in the SPH and SPHS $\times 128$ runs (left and right panels respectively). Qualitatively we see evidence that the projected gas density in the core of the SPH run is higher compared to its SPHS counterpart. The SPH run also contains a number of dense knots of substructure, some of which show evidence of stripping, which are not apparent in the SPHS run.

Spherically Averaged Profiles We make these observations more precise in Figure 3 and 4. In Figure 3 we plot the spherically averaged radial gas density (upper panel) and temperature profiles (lower panel) for the $\times 8$, 32, 128 and 256 resolution runs, including only bins which contain in excess of 10 gas particles (this affects only the innermost bins) down to the gravitational softening scale ϵ_{opt} . For comparison we plot also the dark matter density profile down to the converged radius for the $\times 256$ SPH run. The spherically averaged gas density is systematically lower in the SPHS run when compared to the SPH run at fixed cluster-centric radius, with the disparity increasing with decreasing radius – from ~ 0.4 dex in the outer parts $\gtrsim 10\% R_{\text{vir}}$ to ~ 1.4 dex within the central $10\% R_{\text{vir}}$, in keeping with our observations in Figure 2. The temperature

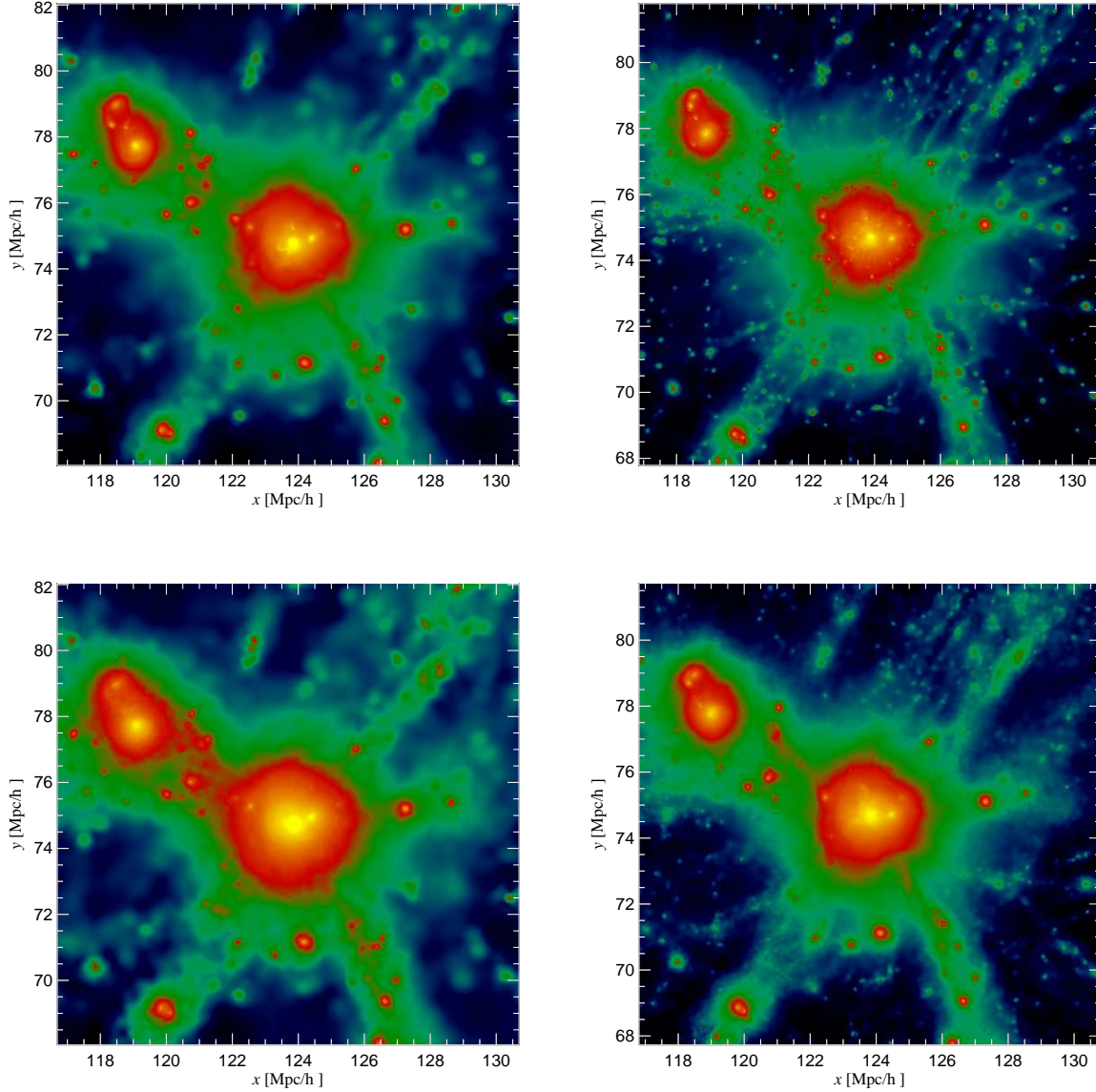


Figure 1. Visual Impression. Projected gas density maps in a cube of side $15 h^{-1} \text{Mpc}$ centred on the cluster at $z=0$ in the $\times 32$ and $\times 128$ SPH (top left and right) and SPHS (bottom left and right) runs respectively.

profiles are in reasonable agreement at large radii ($\gtrsim 20\% R_{\text{vir}}$) for well resolved runs ($\times 32, 128$) but they diverge at small radii by as much as 0.4 dex.

There is good consistency between the gas density profiles in the SPHS runs – to better than 10% to within 0.1 (0.03) R_{vir} for the $\times 8$ (32) runs, compared to $\times 128$. In contrast, the gas density profiles in the SPH runs start to deviate by greater than 10% at 0.2 (0.03) R_{vir} for the $\times 8$ (32) runs, compared to their $\times 128$ counterpart. A similar degree of consistency is evident in the temperature profiles – to better than 10% to within 0.1 (0.02) R_{vir} for the $\times 8$ (32) SPHS runs with respect to the fiducial $\times 128$ SPHS run, and to better than 10% to within 0.3 (0.3) R_{vir} for the $\times 8$ (32) SPH runs with respect to the fiducial $\times 128$ SPH run.

These results show that SPH produces cluster cores that are have higher central densities and lower central temperatures than their counterparts in SPHS, and so we expect systematically lower

entropies in SPH, according to Equation (1). This is evident in Figure 4, in which we compare entropy profiles at $z=0$ in the SPH and SPHS runs – as well as one of the AMR runs, which we shall discuss below. The entropy profiles in the SPH runs are consistent with those report by previous studies, declining with decreasing cluster-centric radius. There is no obvious convergence with increasing mass resolution – the entropy continues to reach smaller values as the mass and spatial resolution improves. In contrast, the entropy profiles plateau to a well-defined value in the SPHS runs and there is excellent agreement between the different resolution runs for $R \gtrsim 0.02 R_{\text{vir}}$. Physically this is not unreasonable – if the cluster is in approximate hydrostatic equilibrium, as we might expect during a period of quasi-dynamical equilibrium, we would expect the central gas density to plateau for both isothermal and polytropic equations of state (cf. Makino et al.

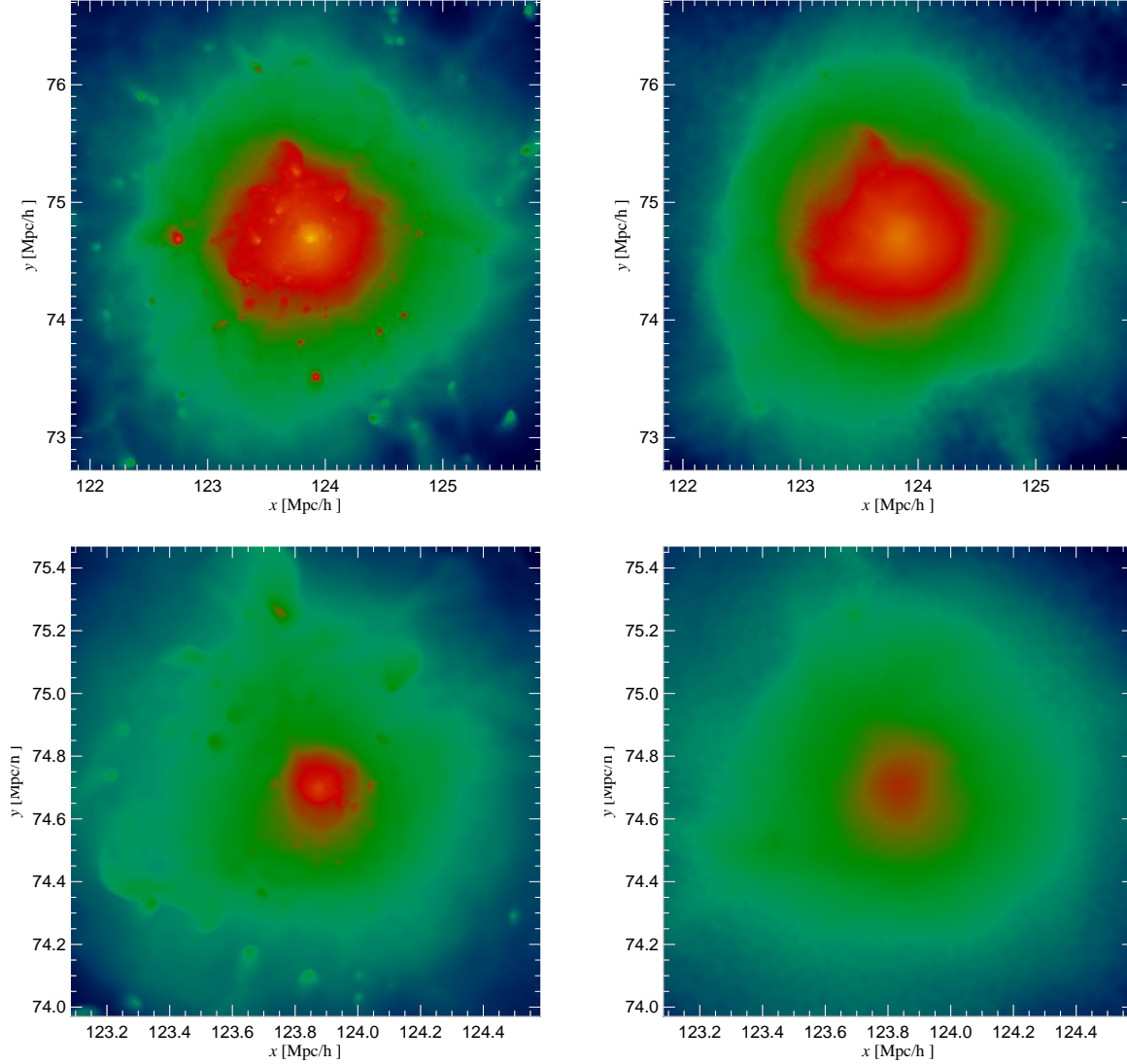


Figure 2. Projected gas density maps of the $\times 128$ SPH and SPHS runs (left and right panels), within cubes of side 5 and $2 h^{-1} \text{Mpc}$ (top and bottom panels) centred on the cluster at $z=0$.

1998; Komatsu & Seljak 2001), with the consequence that the central entropy profile should also plateau.

Sensitivity to Artificial Bulk Dissipation Constant α_{max} . SPHS invokes numerical dissipation in converging fluid flows to suppress multi-valued fluid quantities (e.g. pressure), which lead to large numerical errors. This is controlled by α_{max} , whose default value is 1 and which in the limit of $\alpha_{\text{max}} \rightarrow 0$ should produce results that are more similar to classic SPH (though not identical, since SPHS has improved force accuracy as compared to classic SPH; see §3). Figure 5 provides a visual impression of the SPHS density field, centred on the outskirts of the cluster at $z=1$, in $\times 8$ and 32 runs (top and bottom panels) assuming values of $\alpha_{\text{max}}=1$ and $\alpha_{\text{max}}=5$ (left and right panels respectively). We expect $\alpha_{\text{max}}=5$ runs to be more dissipative than $\alpha_{\text{max}}=1$, and we expect dissipation to shift to smaller scales with increasing mass resolution. These effects, although subtle, are borne out in the left and middle panels of Figure 5 (focus, for example, on the small substructure in the $\times 32$ simulations at $\sim [122.2, 74.8] \text{Mpc/h}$). We quantify this further in

the right panels, by plotting the logarithm of:

$$\kappa(x, y) = \frac{P_1 - P_5}{P_1 + P_5}$$

where $P_{\alpha_{\text{max}}}$ is the value of the pixel at coordinate (x, y) in the run of given α_{max} . Notice that the differences between the $\alpha_{\text{max}}=1$ and $\alpha_{\text{max}}=5$ simulations shift to smaller scales with increasing resolution.

Figure 6 shows the spherically averaged entropy profiles at $z = 0$ in four runs at $\times 8$ resolution – one in which numerical dissipation is switched off (i.e. $\alpha_{\text{max}} = 0$), one set to its default value (i.e. $\alpha_{\text{max}} = 1$), and two with $\alpha_{\text{max}} = 2$ and 5. For $\alpha_{\text{max}} \geq 1$ the profiles are converged; for $\alpha_{\text{max}} = 0$, the profile is declining with decreasing radius, albeit less sharply than the entropy profile from the corresponding $\times 8$ SPH run. These results demonstrate that the differences between SPH and SPHS are largely driven by the numerical dissipation implemented in SPHS, rather than the improved force accuracy.

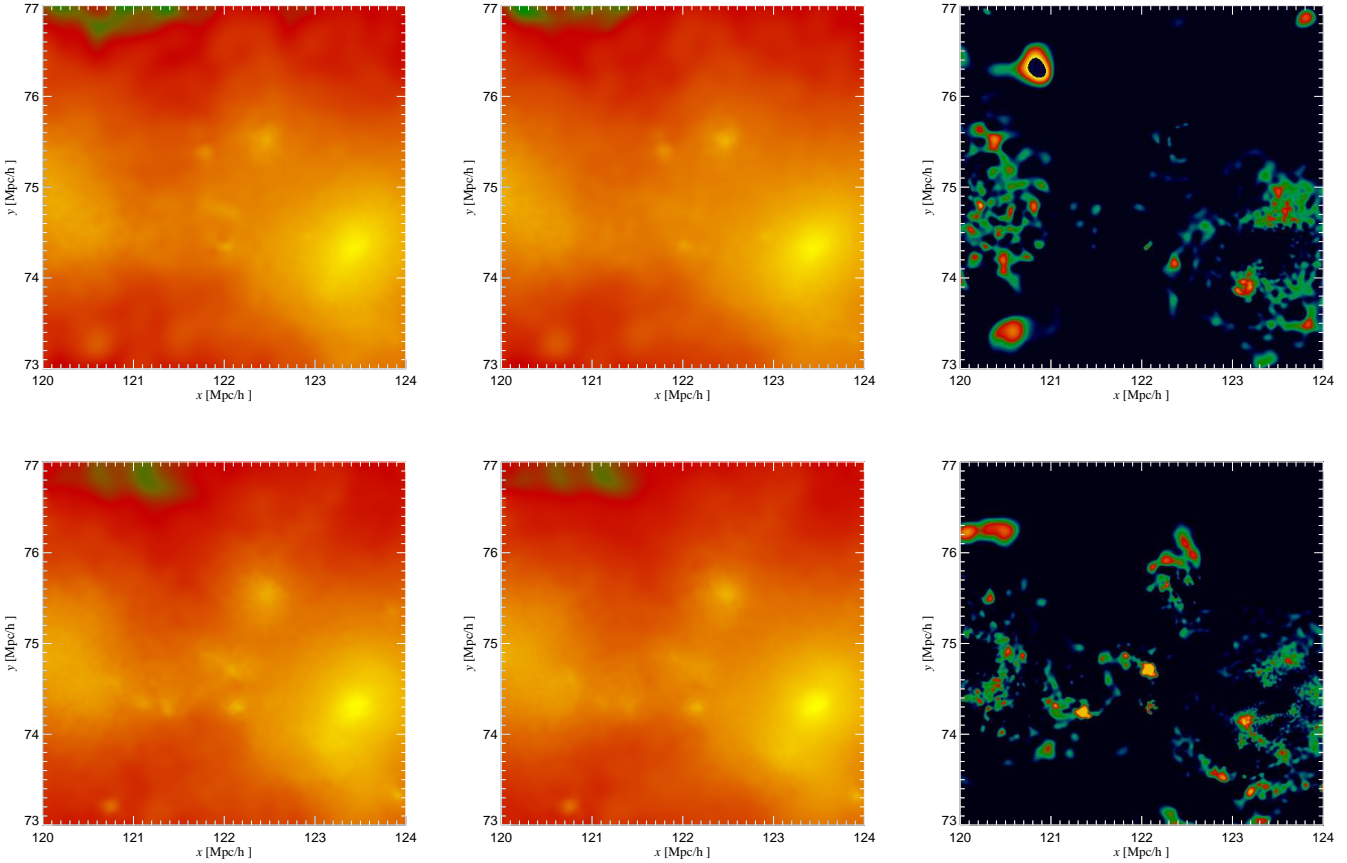


Figure 5. Visual Impression. Maps of the projected gas density in a cube of side $4 h^{-1} \text{Mpc}$ centred on the outskirts of the cluster at $z=1$ in the $\times 8$ and $\times 32$ SPHS runs (top and bottom panels). Left and middle panels show results for runs in which $\alpha_{\text{max}}=1$ and $\alpha_{\text{max}}=5$ respectively; right panels plot $\kappa(x, y) = [P_1 - P_5] / [P_1 + P_5]$, where $P_{\alpha_{\text{max}}}$ is the value of the pixel at (x, y) in the run with given α_{max} .

4.2 Comparison with AMR

We show projected density maps of the gas within a cube of side $15 h^{-1} \text{Mpc}$ centred on the cluster at $z=0$ in the SPH, SPHS and AMR runs in Figure 7. The large-scale spatial distribution of gas is similar across the runs – the cluster forms at the intersection of several filaments that are funneling lower mass systems towards it. It is evident from these density maps, and from comparison of cluster virial masses and merging histories, that we have captured the cluster at a slightly earlier stage of its evolution in the AMR run compared to the SPH and SPHS runs – the cluster has yet to merge with the complex of lower mass structures at projected position $(x, y) \sim (125, 75) h^{-1} \text{Mpc}$ in the AMR run, whereas this merger that occurred at $z \sim 0.14$ in the SPH and SPHS runs. This difference in timing reflects structural differences in the low resolution mass distribution between the GADGET and RAMSES runs, which in turn affects the large-scale gravitational field and consequently halo dynamics.

Despite these differences, we find very good consistency between entropy profiles in the SPHS and AMR runs, as shown in Figure 4. Recall that the SPHS and SPH results – for the $\times 8$, 32, 128 and 256 resolutions – are indicated by heavy and light curves respectively, while the results of the AMR 128 and 256 runs are heavy solid (dotted) curves connecting filled triangles (circles). There is excellent agreement between the two AMR runs, while the level of agreement between the SPHS and AMR runs is impressive – it is as

good as the scatter in the central entropy profile across the different resolution SPHS runs.

This scatter in central entropy in the SPHS and AMR runs is to be expected – we are modelling a chaotic non-linear system and so as our mass and force resolution increases so too does our power to resolve smaller scale perturbations, which will be imprinted on the central entropy profile at later times. However, we do not expect significant changes in the central entropy in either the SPHS or AMR runs as we go to higher mass and force resolution; we may resolve smaller-scale perturbations and form lower mass substructures, but these substructures will find it as difficult, if not more so, to retain their gas, and their lower masses imply that will have correspondingly longer dynamical friction and (consequently) merging timescales.

We can see why by noting that the ram pressure acting on these substructures as they pass close to the cluster core is of order $\rho_{\text{cl}} \sigma_{\text{cl}}^2$, where ρ_{cl} is the central density of the cluster and σ_{cl} is the cluster’s velocity dispersion, and this ram pressure will be effective provided $\rho_{\text{cl}} \sigma_{\text{cl}}^2 \gtrsim \rho_{\text{gas,sub}} \sigma_{\text{sub}}^2$, where $\rho_{\text{gas,sub}}$ is the gas density within the substructure and σ_{sub}^2 is the substructure’s velocity dispersion. Lower mass substructures will be more concentrated and so will have higher gas densities (i.e. $\rho_{\text{gas,sub}} > \rho_{\text{cl}}$), but the rate of increase of concentration with decreasing mass is a very weak function of mass (e.g. $\sim M^{-0.1}$, cf. Neto et al. 2007) and so, in the absence of cooling, the decrease in σ dominates; lower mass sub-

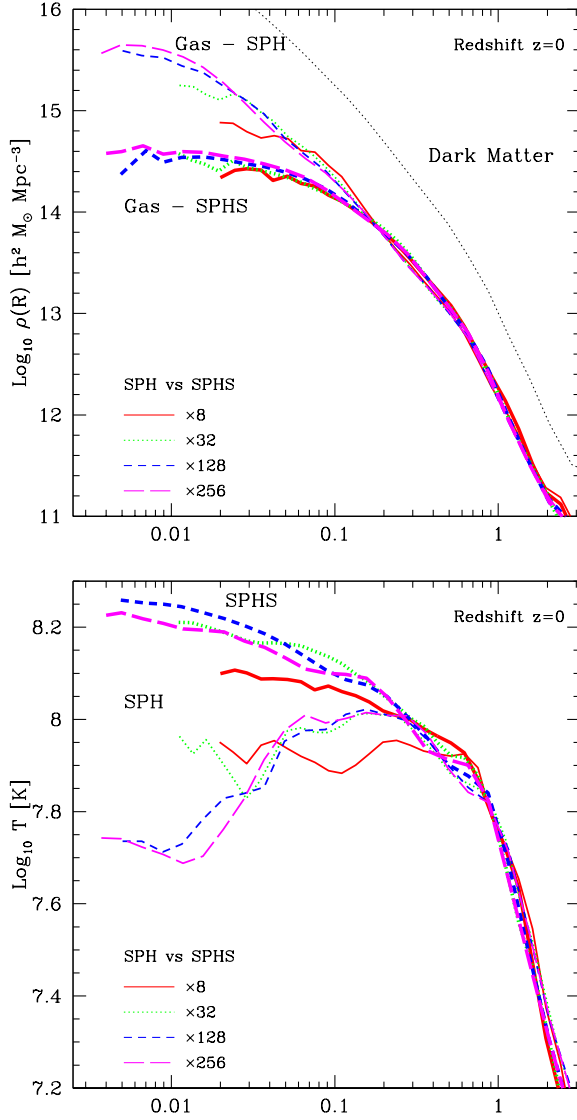


Figure 3. Spherically averaged density (upper panel) and mass-weighted temperature profiles (lower panel) at $z=0$. The heavy (SPHS) and light (SPH) solid, dotted, short dashed and long dashed curves correspond to the $\times 8$, 32, 128 and 256 runs, plotted down to the gravitational softening ϵ_{opt} . The light dotted curve in the upper panel corresponds to the dark matter density profile in the $\times 256$ SPH run.

structures become progressively more susceptible to ram pressure stripping.

If anything, the presence of this population of substructures will be more of a blight for the classic SPH runs, because they are more likely to retain their gas and the passage of these cooler clumps through the cluster core will lead to more frequent shocking and stirring, leading to fluctuations in the central entropy that may not be evident in lower resolution runs.

4.3 Redshift Evolution

So far, we have compared cluster properties at $z = 0$ in the SPH, SPHS and AMR runs. We now consider cluster properties at earlier times, whose evolution we distill in Figure 8. Here we show how the spherically averaged estimates of the entropy, density and tem-

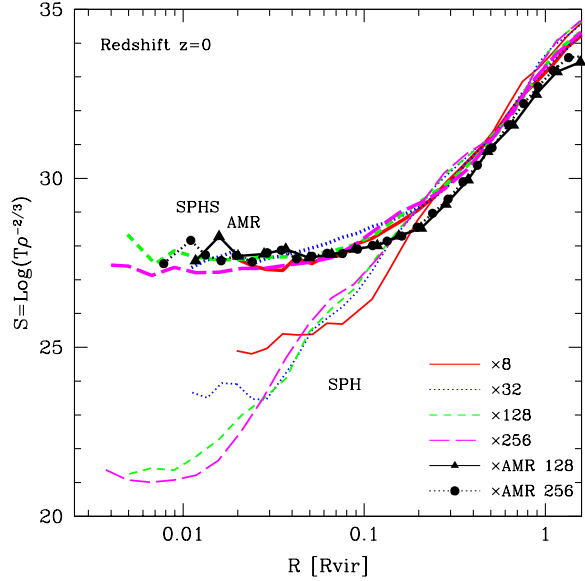


Figure 4. Spherically averaged entropy profiles measured at $z = 0$. The heavy (SPHS) and light (SPH) solid, dotted, short dashed and long dashed curves correspond to the $\times 8$, 32, 128 and 256 resolution runs, plotted down to the gravitational softening ϵ_{opt} . Overplotted are the results of the AMR 128 and 256 runs – heavy solid (dotted) curves connecting filled triangles (circles). See text for further discussion.

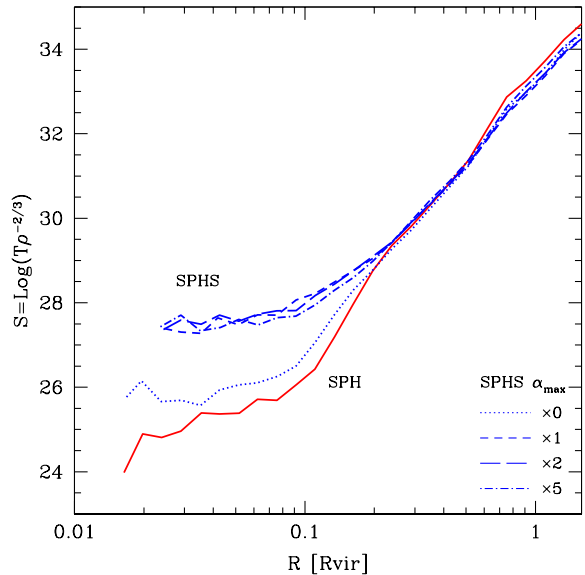


Figure 6. Sensitivity to Artificial Bulk Dissipation Constant α_{max} . Spherically averaged entropy profiles assuming dissipation is switched off (i.e. $\alpha_{\text{max}}=0$; dotted-dashed curve); switched on and set to its default value (i.e. $\alpha_{\text{max}}=1$; long dashed); and switched on and set to $\alpha_{\text{max}}=2$ and 5 (short dashed and dotted respectively). For comparison we show also the profile from the corresponding classic SPH run (solid curve).

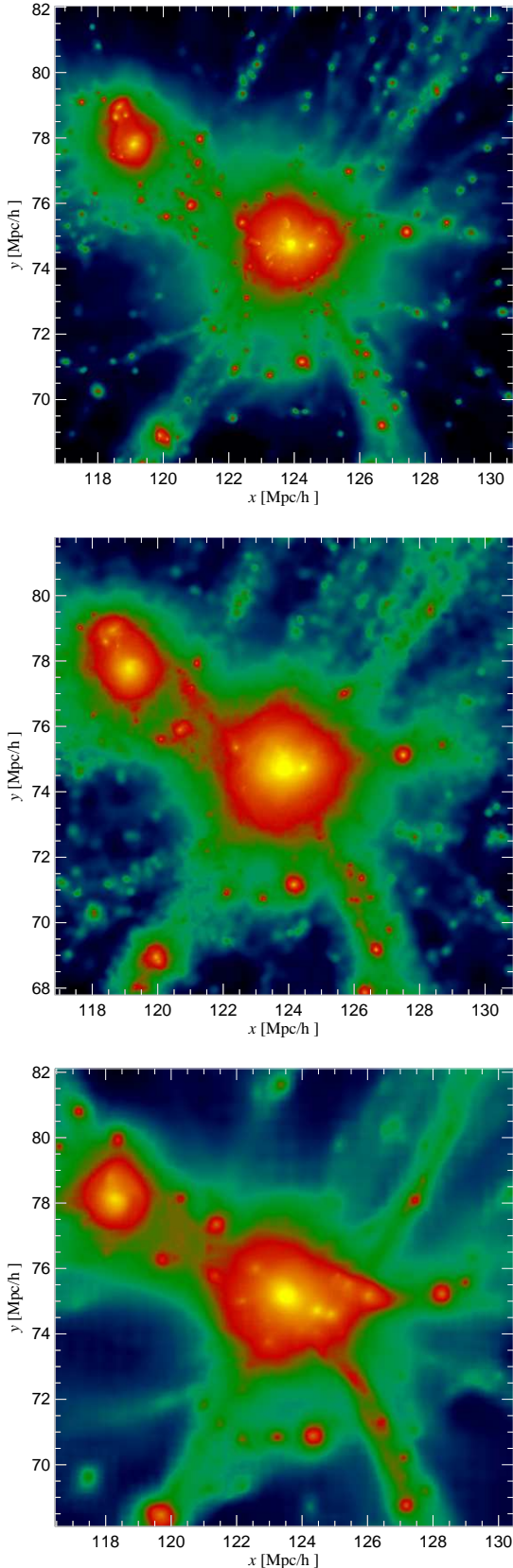


Figure 7. Code Comparison: Visual Impression Projected gas density maps in the SPH, SPHS and AMR runs (from top to bottom) within a $15 h^{-1} \text{Mpc}$ cube centred on the cluster at $z = 0$.

perature (top, middle and bottom panels), measured at a fiducial radius $R_{0.01}=0.01R_{\text{vir}}$, have varied with redshift since $z \sim 1$. Results from the $\times 256$ SPH and SPHS runs are indicated by crosses and filled squares; filled triangles correspond to the results from the AMR256 run.

This is a revealing figure for a number of reasons. First, it indicates that the SPH and SPHS runs produced broadly consistent results at $z \gtrsim 0.6$, but have diverged since then such that there is a factor of 10 (3) difference in the estimated density (temperature) at $z=0$. If we look at the spherically averaged profiles in detail at, say, $z \sim 1$ (cf. Figure 9) we find that a plateau can form in the SPH entropy profile (cf. the $\times 256$ run) and there can be reasonable consistency between the SPH and SPHS profiles, but this plateau is a transient feature in the SPH case whereas it is long-lived in the SPHS case, and it is also resolution dependent (compare the $\times 256$ profile to the $\times 8, 32$ and 128 profiles, which are declining with radius).

This relates to our second observation, which is the relative stability of the SPH entropy profile compared to the SPH entropy profile; since $z = 1.2$, $S_{0.01} \sim 28$ in the SPHS run whereas $S_{0.01}$ has fluctuated and spanned the range $22 \lesssim S_{0.01} \lesssim 28$. These fluctuations track the violent assembly history of the cluster; it has a formation redshift⁶ of $z_{\text{form}} = 0.5$, which is typical for the most massive galaxy clusters, and it has assembled 70% of its $z = 0$ mass since $z = 1$. As noted earlier, a key difference between the SPH and SPHS runs is the abundance of low mass, high density clouds evident in the SPH density field that are not present in the SPHS density field. These clouds are associated low entropy material in the cores of underlying dark matter substructures; as they plunge towards the cluster centre and merge, gas is stripped and flung outwards, shocking to high temperatures. The low entropy material settles in the cluster core and gives rise to the lower entropy profile evident at $z = 0$, but the shocked gas in the cluster core takes time to expand and redistribute, stirring the cluster gas in the process. The same dark matter substructures are evident in the SPHS and AMR runs, but if they are occupied by gas it is at a higher entropy and so is more easily stripped by the intra-cluster medium.

Third, we note excellent consistency between the SPHS and AMR runs holds at earlier times. This is also evident in the entropy profiles (cf. Figure 9).

5 DISCUSSION

5.1 What is the origin of the discrepancy between the classic SPH and the AMR results?

Since the work of Frenk et al. (1999), it has been known that SPH and AMR codes produce very different results for the entropy profile of the intracluster medium in non-radiative simulations of a massive galaxy cluster. Numerous studies in the literature have suggested that the SPH results are flawed (Wadsley et al. 2008; Mitchell et al. 2009; Sijacki et al. 2011), most likely owing to a spurious numerical surface tension (Agertz et al. 2007). Indeed, a recent simulation using SPH with dissipation in entropy has reported an entropy core more similar to that found in AMR or mesh-based simulations (Wadsley et al. 2008). However, the amplitude

⁶ Following convention, we define the formation redshift cluster as the redshift at which half its $z = 0$ virial mass is in place (cf. Power et al. 2012, and references therein)

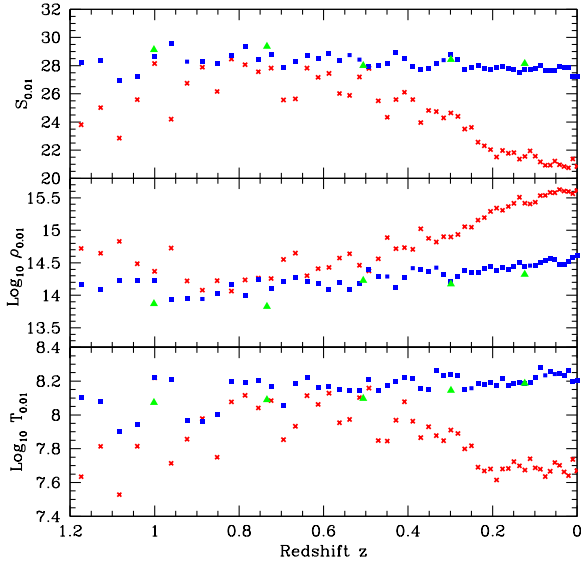


Figure 8. Redshift variation of the spherically averaged entropy $S_{0.01}$, density $\rho_{0.01}$ and temperature $T_{0.01}$ (upper, middle and lower panels) measured at a fiducial cluster-centric radius of $0.01 R_{\text{vir}}$. Crosses, filled squares and filled triangles correspond to SPH, SPHS and AMR results.

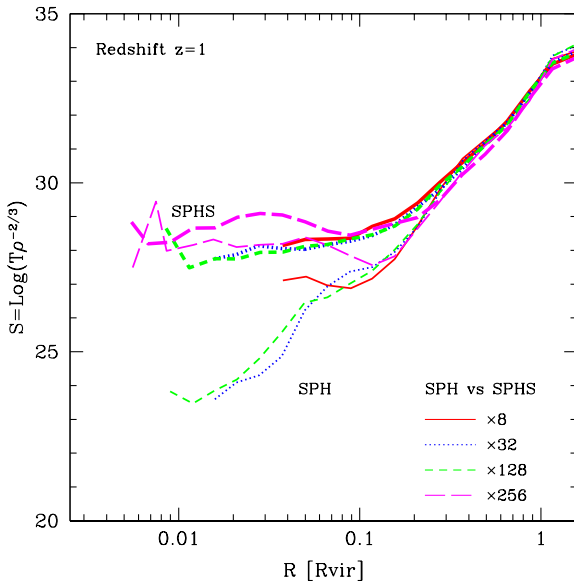


Figure 9. Spherically averaged entropy profiles at $z=1$. As in Figure 4, the heavy (SPHS) and light (SPH) solid, dotted, short dashed and long dashed curves correspond to the $\times 8$, 32, 128 and 256 resolution runs, plotted down to the gravitational softening ϵ_{opt} .

of this core was found to be sensitive to both the choice of numerical dissipation parameters and the numerical resolution (see §5.2 for further discussion of this). In this paper, we have tested a new SPH algorithm – SPHS – that is designed to converge with increasing resolution independently of the choice of dissipation parameters (Read & Hayfield 2012); we also present explicit comparisons with an AMR code RAMSES, similarly to the original study of (Frenk et al. 1999). Our suite of simulations that explore resolution,

dissipation parameter and choice of hydrodynamic solver allow us to pin-point the precise reasons for the differences between the SPH and AMR simulations.

At high redshift, $z \sim 1$, there are already significant differences between the codes. Although SPH agrees qualitatively with SPHS and AMR at these early times, there is significantly more scatter between simulations of differing resolution. As the resolution is increased, the entropy core in SPH fluctuates significantly in amplitude by a factor up to ~ 150 (cf. Figure 9), suggesting non-convergent behaviour. This can be traced to the spurious surface tension reported originally in Agertz et al. (2007). As detailed in Read et al. (2010) and Read & Hayfield (2012), this owes to multi-valued pressures at phase boundaries, such as arise when substructures containing lower entropy gas pass through the cluster core, shocking and stirring the gas. Since these drive pressure waves through the fluid, this propagates numerical errors away from regions of converging flow to the whole fluid domain (cf. Figure 10; pressure discontinuities are more pronounced in the SPH run). By contrast, in SPHS we introduce numerical dissipation when the flow is converging *designed to ensure single valued pressures* (and indeed to ensure all fluid quantities are single-valued). This keeps errors local, ensuring that they shift to smaller scales with increasing numerical resolution and, thereby, guaranteeing numerical convergence.

At low redshift $z = 0$, the SPH results appear to converge on an ever lower central entropy. However, this illusion of convergence is actually driven by low entropy gas that artificially sinks to the cluster centre, protected by its numerical surface tension. This is masked at high redshift by on-going mergers that drive shocks and entropy generation in the gas. Note that dialling the entropy dissipation in SPHS down to zero, we find results that are similar to those from classic SPH (see figure 6). This demonstrates that the differences between SPHS and AMR are driven largely by the numerical dissipation rather than the improved force accuracy in SPHS.

5.2 Do resolved scales in non-radiative simulations of galaxy cluster formation care about the details of dissipation (physical or numerical) on unresolved scales?

A key advantage of SPHS is that we can control the numerical dissipation, dialling it both up and down. This allows us to measure the impact of unresolved dissipative processes on resolved scales in the simulations. It has already been reported that numerical dissipation on small scales can affect the size and magnitude of a central entropy core (Wadsley et al. 2008). However, there is a key difference between the dissipation added in Wadsley et al. (2008) and that in SPHS. Wadsley et al. (2008) build a simple sub-grid model for unresolved turbulence as a physical driver of dissipation at the resolution limit. Similar but more sophisticated attempts at the same have also been conducted by (Maier et al. 2009). Such sub-grid turbulence acts everywhere in the simulation and appears at first sight desirable as it seeks to capture unresolved physics. Indeed, Maier et al. (2009) report a higher normalisation for entropy cores in their simulations that include a sub-grid turbulence model, suggesting that such sub-grid turbulence may well impact on resolved scales in galaxy cluster simulations. However, Maier et al. (2009) do not perform any numerical convergence tests. Thus it is not clear whether the entropy core they report in either case – with or without sub-grid turbulence – is a numerically robust solution. Indeed, Wadsley et al. (2008) show that the amplitude of the entropy core that they form, at fixed numerical dissipation param-

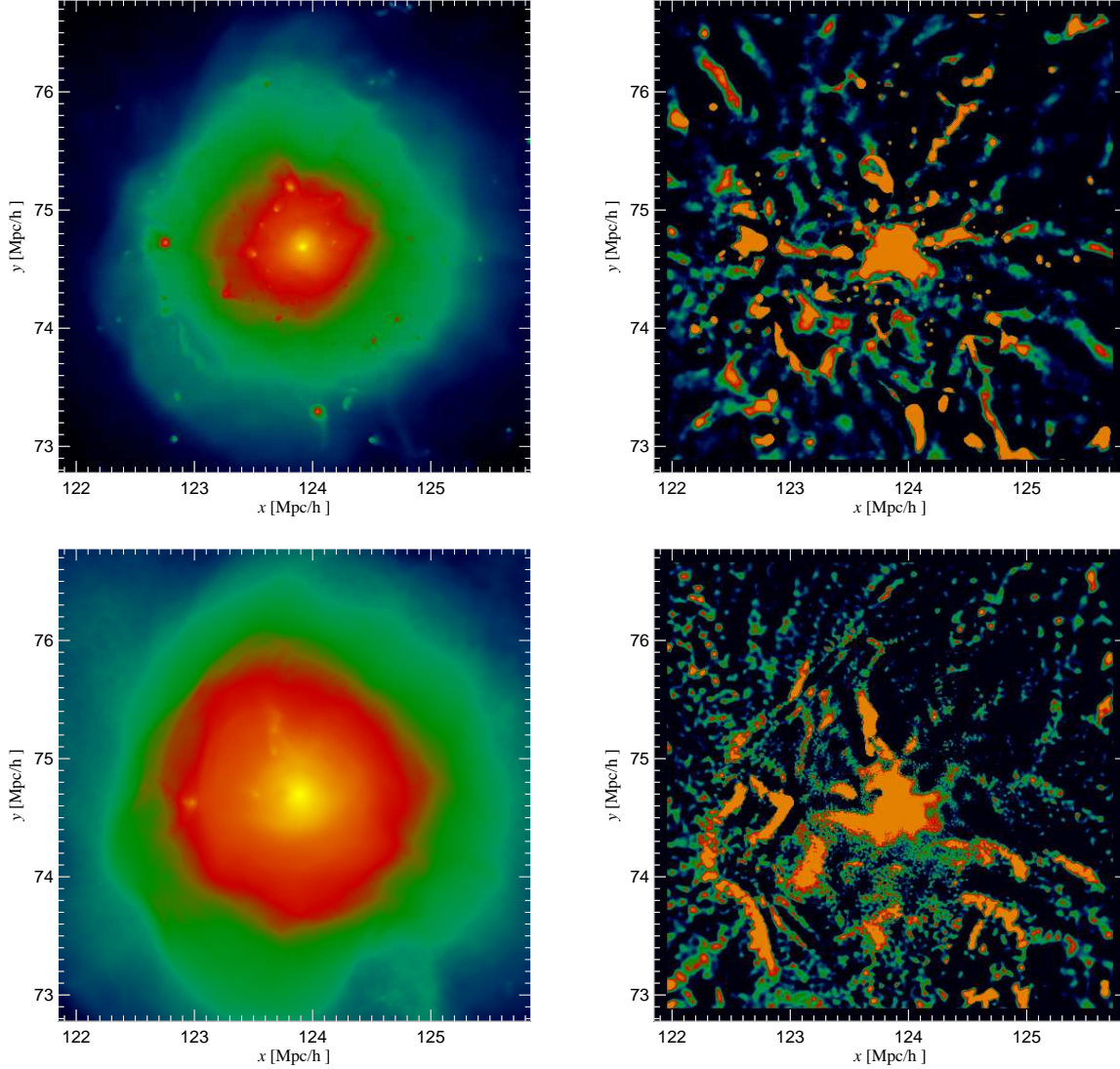


Figure 10. Pressure Discontinuities in SPH. Projected pressure maps in the SPH (top left) and SPHS (bottom left) $\times 256$ runs within a $4 h^{-1} \text{Mpc}$ cube centred on the cluster at $z = 0$. SPH produces sharp pressure discontinuities associated with orbiting substructures; these are evident in the right panels, which are obtained by unsharp masking (i.e. subtracting a smoothed version of the projected pressure map to highlight residual structures).

ter, decreases with increasing resolution⁷. This underscores the key problem with sub-grid turbulence models: there is no guarantee that they will produce a faithful convergence on the continuum Euler equations. By contrast, the dissipation in SPHS is *numerical*. It is required in order to ensure single-valued fluid quantities throughout the flow, but is otherwise kept to a minimum. The situation is similar in the RAMSES code where minimal (and therefore unavoidable) numerical dissipation follows from the Riemann solver (e.g.

⁷ The effect is smaller if small-scale waves are omitted from the higher resolution simulation, but convergence is not convincingly shown. There are also some oddities. With a very large diffusion coefficient ($C=10$) at fixed resolution, they actually form a *lower* amplitude core than that formed with intermediate values (see their figure 12). Although such values for the diffusion coefficient are unphysically large, this counter-intuitive behaviour may reflect the limitations of the simplified sub-grid turbulence model employed.

van Leer 1979). In both cases, we expect a rigorous convergence on the continuum Euler equations with increasing resolution.

The works of Wadsley et al. (2008) and Maier et al. (2009) leave a dangling question mark over whether or not it is useful – or indeed essential – to build physically motivated sub-grid turbulence models, or whether we can be satisfied with simply keeping numerical dissipation to a minimum and performing numerical convergence studies. We can address this point using SPHS by dialling up α_{max} to large values and seeing how this impacts results on resolved scales. This is shown in figure 6. Notice that the results for the entropy profile of the gas are in excellent agreement even for very large values of $\alpha_{\text{max}} = 5$. Visual inspection of the gas density profiles show that the $\alpha_{\text{max}} = 5$ simulation is significantly more dissipative than the $\alpha_{\text{max}} = 1$ default case. However, such dissipation shifts to smaller scales with increasing resolution and the equivalent comparison at $\times 32$ resolution shows even fewer differences: the results for SPHS converge independently of our choice of α_{max} (cf. Figure 5). Furthermore – despite the very different na-

ture of the errors, error propagation, and numerical dissipation – the SPHS simulations converge on a solution in remarkable accord with the AMR simulation (see figure 8).

Our results suggest that while numerical dissipation is necessary in any numerical method, so long as it is kept to a minimum its effect on non-radiative galaxy cluster simulations is benign. Furthermore, there appears to be no requirement to physically model sub-grid dissipation processes. Indeed, doing so may even be undesirable if it leads to a spurious transfer of information from unresolved to resolved scales. This could spoil convergence, preventing a correct solution of the Euler equations in the continuum limit.

5.3 What is the role of gravitational shock heating as an entropy generation mechanism in galaxy clusters?

Real galaxy clusters in the Universe are known to split into two types: CC and NCC (see §1). Armed with our results from SPH, SPHS and AMR we can now return to the question of the physical origin of this dichotomy. It is clear that in the absence of radiative cooling, entropy cores consistent with NCC clusters form, with the entropy generated from shocked gas during the cluster assembly process. It is likely, however, that real NCC clusters result from a more complex interplay between heating and cooling in the cluster core (McCarthy et al. 2008). While it is beyond the scope of this work to fully explain the observed dichotomy between NCC and CC clusters in nature, we have laid the foundations for such a study. Understanding the numerically well-defined problem of non-radiative galaxy clusters allows us to move with confidence to more physically realistic simulations that model also cooling, star formation and feedback from supernovae and active galactic nuclei. This will be the subject of forthcoming papers.

6 CONCLUSIONS

We have studied the entropy profile of the intracluster medium in a massive galaxy cluster forming in a non-radiative hydrodynamical cosmological resimulation using classic SPH, SPHS and AMR codes. In common with previous studies, we find that SPH entropy profiles decline with decreasing cluster-centric radius, whereas SPHS and AMR entropy profiles are in excellent agreement, plateauing to a well-defined value. Our key conclusions are as follows:

(i) The classic SPH result is incorrect, owing to a known artificial surface tension that appears at phase boundaries. At early times, the passage of massive substructures close to the cluster centre shock and stir gas, building up an entropy core. At late times, the artificial surface tension causes low entropy gas – that ought to mix with the higher entropy gas – to sink artificially to the centre of the cluster.

(ii) Provided numerical dissipation occurs only at the resolution limit, and provided that it does not propagate errors to larger scales, we find that the effect of numerical dissipation is benign. There is no requirement to build ‘sub-grid’ models of unresolved turbulence for galaxy cluster simulations.

(iii) Entropy cores in non-radiative simulations of galaxy clusters are physical, resulting from entropy generation in shocked gas during the cluster assembly process. This finally puts to rest the long-standing puzzle of cluster entropy cores in AMR simulations versus their apparent absence in classic SPH simulations.

ACKNOWLEDGEMENTS

CP thanks Aaron Robotham for helpful conversations during the writing of this paper. The simulations presented in this paper were run on the iVEC EPIC and NCI VAYU supercomputers. The research presented in this paper was undertaken as part of the Survey Simulation Pipeline (SSimPL; <http://ssimpl-universe.tk/>). JIR acknowledges support from SNF grant PP00P2_128540/1.

This paper has been typeset from a \TeX / \LaTeX file prepared by the author.

REFERENCES

- Abel T., 2011, MNRAS, pp 196–
- Agertz O., Moore B., Stadel J., Potter D., Miniati F., Read J., Mayer L., Gawryszczak A., Kravtsov A., Nordlund Å., Pearce F., Quilis V., Rudd D., Springel V., Stone J., Tasker E., Teyssier R., Wadsley J., Walder R., 2007, MNRAS, 380, 963
- Berger M. J., Colella P., 1989, Journal of Computational Physics, 82, 64
- Berger M. J., Oliger J., 1984, Journal of Computational Physics, 53, 484
- Bryan G. L., Norman M. L., 1997, in Clarke D. A., West M. J., eds, Computational Astrophysics; 12th Kingston Meeting on Theoretical Astrophysics Vol. 123 of Astronomical Society of the Pacific Conference Series, Simulating X-Ray Clusters with Adaptive Mesh Refinement. p. 363
- Bryan G. L., Norman M. L., Stone J. M., Cen R., Ostriker J. P., 1995, Computer Physics Communications, 89, 149
- Cavaliere A., Fusco-Femiano R., 1976, A&A, 49, 137
- Cullen L., Dehnen W., 2010, MNRAS, 408, 669
- Dehnen W., Aly H., 2012, ArXiv e-prints
- Dehnen W., Read J. I., 2011, European Physical Journal Plus, 126, 55
- Dilts G., 1999, International journal for numerical methods in engineering, 44, 1115
- Dolag K., Vazza F., Brunetti G., Tormen G., 2005, MNRAS, 364, 753
- Frenk C. S., White S. D. M., Bode P., Bond J. R., Bryan G. L., Cen R., Couchman H. M. P., Evrard A. E., Gnedin N., Jenkins A., Khokhlov A. M., Klypin A., Navarro J. F., Norman M. L., Ostriker J. P., Owen J. M., Pearce F. R., 8 other authors. 1999, ApJ, 525, 554
- Fryxell B., Olson K., Ricker P., Timmes F. X., Zingale M., Lamb D. Q., MacNeice P., Rosner R., Truran J. W., Tufo H., 2000, ApJS, 131, 273
- Gaburov E., Nitadori K., 2010, ArXiv e-prints
- Gingold R. A., Monaghan J. J., 1977, MNRAS, 181, 375
- Giodini S., Pierini D., Finoguenov A., Pratt G. W., Boehringer H., Leauthaud A., Guzzo L., Aussel H., Bolzonella M., Capak P., Elvis M., Hasinger G., other authors., the COSMOS Collaboration 2009, ApJ, 703, 982
- Gunn J. E., Gott J. R. I., 1972, ApJ, 176, 1
- Heß S., Springel V., 2010, MNRAS, 406, 2289
- Hobbs A., Read J., Power C., Cole D., 2012, ArXiv e-prints
- Hopkins P. F., 2013, MNRAS, 428, 2840
- Hughes J. P., 1989, ApJ, 337, 21
- Inutsuka S.-I., 2002, Journal of Computational Physics, 179, 238

- Kawata D., Okamoto T., Gibson B. K., Barnes D. J., Cen R., 2013, MNRAS, 428, 1968
- Khokhlov A., 1998, Journal of Computational Physics, 143, 519
- Knollmann S. R., Knebe A., 2009, ApJS, 182, 608
- Komatsu E., Seljak U., 2001, MNRAS, 327, 1353
- Lucy L. B., 1977, AJ, 82, 1013
- Maier A., Iapichino L., Schmidt W., Niemeyer J. C., 2009, ApJ, 707, 40
- Makino N., Sasaki S., Suto Y., 1998, ApJ, 497, 555
- Maron J. L., Howes G. G., 2003, ApJ, 595, 564
- Mayer L., Governato F., Kaufmann T., 2008, Advanced Science Letters, 1, 7
- McCarthy I. G., Babul A., Bower R. G., Balogh M. L., 2008, MNRAS, 386, 1309
- Mitchell N. L., McCarthy I. G., Bower R. G., Theuns T., Crain R. A., 2009, MNRAS, 395, 180
- Monaghan J. J., 1992, ARA&A, 30, 543
- Murante G., Borgani S., Brunino R., Cha S.-H., 2011, MNRAS, 417, 136
- Neto A. F., Gao L., Bett P., Cole S., Navarro J. F., Frenk C. S., White S. D. M., Springel V., Jenkins A., 2007, MNRAS, 381, 1450
- O'Shea B. W., Nagamine K., Springel V., Hernquist L., Norman M. L., 2005, ApJS, 160, 1
- Power C., Knebe A., Knollmann S. R., 2012, MNRAS, 419, 1576
- Power C., Navarro J. F., Jenkins A., Frenk C. S., White S. D. M., Springel V., Stadel J., Quinn T., 2003, MNRAS, 338, 14
- Price D. J., 2008, J. Comp. Phys., 227, 10040
- Read J. I., Hayfield T., 2012, MNRAS, 422, 3037
- Read J. I., Hayfield T., Agertz O., 2010, MNRAS, 405, 1513
- Ritchie B. W., Thomas P. A., 2001, MNRAS, 323, 743
- Saitoh T. R., Makino J., 2013, ApJ, 768, 44
- Scannapieco C., Wadepuhl M., Parry O. H., Navarro J. F., Jenkins A., Springel V., Teyssier R., Carlson E., Couchman H. M. P., Crain R. A., Dalla Vecchia C., Frenk C. S., Kobayashi C., Monaco P., 9 other authors. 2012, MNRAS, 423, 1726
- Sijacki D., Vogelsberger M., Keres D., Springel V., Hernquist L., 2011, ArXiv e-prints
- Sijacki D., Vogelsberger M., Kereš D., Springel V., Hernquist L., 2012, MNRAS, 424, 2999
- Springel V., 2005, MNRAS, 364, 1105
- Springel V., 2010, MNRAS, 401, 791
- Springel V., Frenk C. S., White S. D. M., 2006, Nature, 440, 1137
- Springel V., Hernquist L., 2002, MNRAS, 333, 649
- Teyssier R., 2002, A&A, 385, 337
- Thacker R. J., Couchman H. M. P., 2000, ApJ, 545, 728
- van Leer B., 1979, Journal of Computational Physics, 32, 101
- Vazza F., 2011, MNRAS, 410, 461
- Vikhlinin A., Kravtsov A., Forman W., Jones C., Markevitch M., Murray S. S., Van Speybroeck L., 2006, ApJ, 640, 691
- Voit G. M., 2005, Reviews of Modern Physics, 77, 207
- Voit G. M., Kay S. T., Bryan G. L., 2005, MNRAS, 364, 909
- Wadsley J. W., Veeravalli G., Couchman H. M. P., 2008, MNRAS, 387, 427
- White S. D. M., Rees M. J., 1978, MNRAS, 183, 341